Active tectonics of the Burma region analysed by kinematic inversion of relative motion data

Gino Battistella

March 2021

Abstract

The Burma terrane is caught in between the hyper-obliquely subducting rigid Indian plate in the West and the Eurasian plate and the Sunda plate in the North- and South-East respectively. As a result, the sandwiched Burma terrane is expected to undergo internal deformation. Due to the obliquity of this subducting Indian plate the Burma slab is hypothesised to be subjected to (mainly) trench-parallel slab dragging. We would like to asses the current geodynamic setting of the Burma slab in the context of India-Eurasia convergence and the motion of the Burma slab and its potential indentation with Eurasia in the Eastern Syntaxis expressed in the deformation field of the crust. For this assesment we have combined GPS data from 1371 stations and applied the Spakman-Nyst method to estimate a deformation field for the Burma region. Our preferred model relies on both, fault slip and continuous deformation. Our model shows significant fault slip on the Sagaing fault and the Rakhine-Bangladesh megathrust with a strain rate in the order of 1E-7/y along the main frontal thrust and at the northern part of the Rakhine-Bangladesh megathrust. A clockwise rotation of up to 5.7°/my is found for North Burma. Our results suggest uplift in the Himalayas and in the Indo-Burman ranges due to active convergence between both India-Eurasia and India-Burma, crustal thinning across the central Tibetan plateau, and NE dragging of the Burma plate by the subducting Indian slab driving plate collision and the CW rotation of the Burma plate.

1 Introduction

The plate subduction history between the Indian and Eurasian plates is complicated and culminated in major continental collision in the early Miocene after which the Indian lithosphere continued to move northward (van Hinsbergen et al. 2019). The boundary of the north-easterly, obliquely converging Indian plate with the Burmese plate can be marked in the Indo-Burmese Ranges (IBR). This obliquity has been related to a significant clockwise rotation of the Burma terrane between 80 and 50 Ma (Westerweel et al., 2019), but the precise tectonic pathway of the Burma terrane is still uncertain. It has been suggested (Rao and Kumar, 1999) that nowadays a significant part of relative motion is the result of horizontal strike-slip faulting, questioning whether subduction is still occurring at all. The particular area of interest for this research is the complex tectonic area surrounding the Burma Arc. Figure 1 shows a recent tectonic map of the Burma Arc region containing the major regional faults, tectonic boundaries and GPS vectors (Mallick et al., 2019). A major north-south oriented dextral strike-slip fault, the Sagaing fault, can be observed. This fault is accountable for a shear motion taking up to about 21 mm/yr, adding to the suggestion of Rao and Kumar (1999). Due to the obliquity of the subducting Indian plate the Burma slab is hypothesized to be subjected to an interesting phenomenon called slab dragging. Slab dragging is defined as the lateral transport of the subducting slab by the absolute motion of the subducting (Indian) plate (Spakman et al. 2018). The possible impact of this process on the overriding plate (Burma) renders a fascinating research topic which is investigated here by kinematic inversion of observed regional crustal motions.

The kinematic inversion method from Spakman and Nyst (2002), hereafter S-N method, analyzes relative motion data acquired, e.g., with the Global Positioning System (GPS). It will be applied to the Burma region to investigate the active tectonics of this region and of its relations to the region's geodynamic setting. The kinematic inversion of relative motion data, and therefore the data itself, is at the core of our research. To optimize obtaining accurate results, all available surface velocity estimates, gathered through published geodetic studies in south-east Asia, will be compiled into one large data set to be used for inversion. The S-N method requires us to solve a forward problem followed by a linear inverse problem. The forward problem uses the relative motion between pairs of GPS stations to estimate the velocity gradient field, relative network rotations, and fault slip rate.

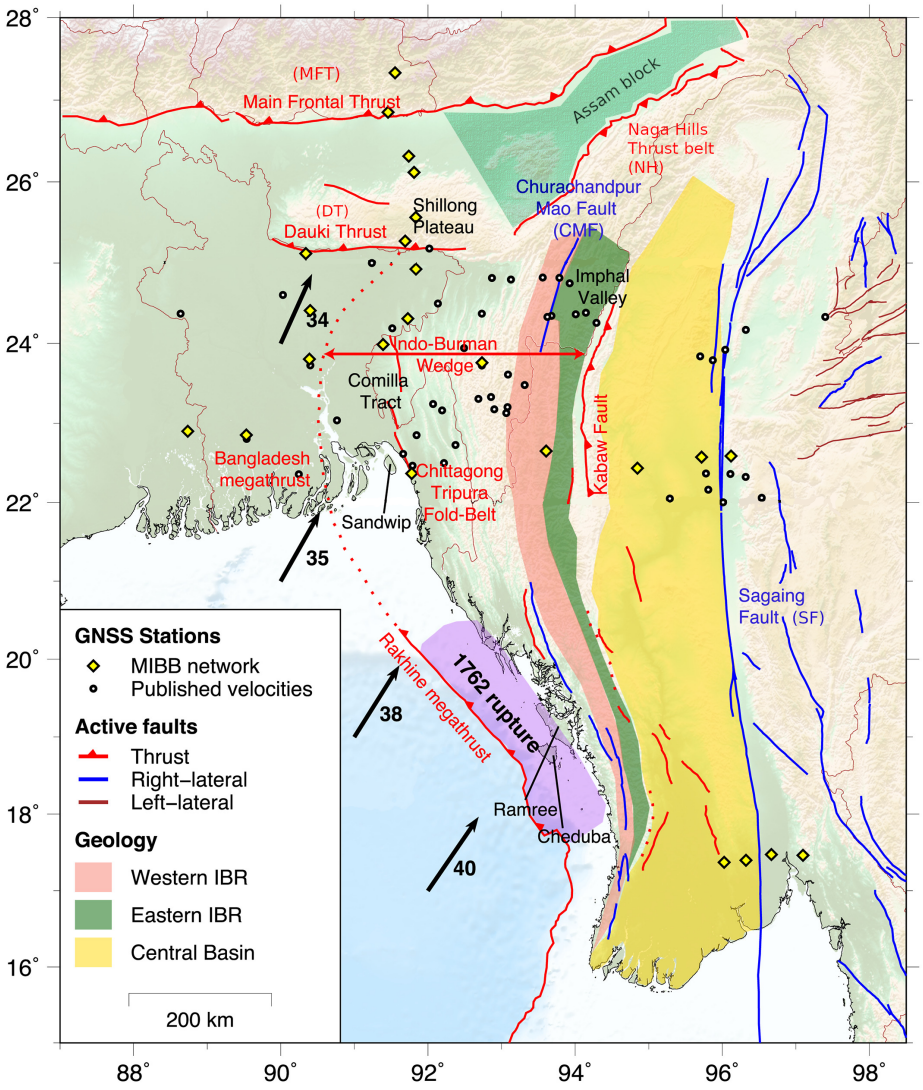

Figure 1: Tectonic map of the Burma region. Tectonic boundaries of the Indian plate are marked by the Main Frontal Thrust, the Naga hills thrust belt and the Banglades-Rakine megathrust. The Indo Burman Ranges (IBR) are divided into the western IBR and eastern IBR based on their geology. The black arrows show the direction and magnitude (mm/year) of motion of India with respect to the Shan block. The location of the Assam block is highlighted in turquoise. Abbreviations of important faults are as follows; CMF = Charachandpur Mao Fault, DT = Dauki Thrust, KBF= Kabaw Fault, MFT = Main Frontal Thrust, NH = Naga Hills Thrust belt, RBMT = Rakhine-Bangladesh Mega Thrust, SF = Sagaing Fault, . Figure taken and adjusted from Mallick et al., 2019. Active convergence of the India-Burma-Sunda plates revealed by anew continuous GPS network. Journal of Geophysical Research: Solid Earth, 124(3), pp.3155-3171

Through this method other results such as the strain- and rotation rate fields can also be derived, which, together with fault motions, provide insight into the active deformation of the region.

The aim of this research is to develop a better geodynamical understanding of the Burma region by linking geological and geophysical observations to the present-day deformation fields as modelled with the S-N method. Large scale faults located in the Burma region have been identified from the literature and are implemented in our inversion model. Resulting strain rates as well as fault creep will be compared to results from previous studies. Finally, we also aim to compare the rotation rate field to rotations in paleomagnetic data to see if there is any similarity between the two.

2 Geodynamic setting

Abbreviations corresponding to their respective fault/system can be found in Figure 1 (Burma) and Figure 3 (Tibetan plateau)

2.1 Himalayan orogenetic belt

The beginning of the Himalayan orogeneses can be marked by the India-Eurasian collision at roughly 58 Ma (van Hinsbergen et al. 2019). A kinematic reconstruction of the evolution of the Himalayan orogenese can be found in figure 2. The Himalayan belt has a massive 2,000 km east-west length and is comprised of 8 large geological units. Since the Himalayas span such a vast length it is no surprise that the western, central and eastern Himalayas show a notable difference in geological construction. However, 4 main units can be observed in all of them (from south to north): The outer Himalayas (sub-Himalayan sequence) are delimited by the Main Frontal Thrust (MFT) and the Main Boundary Thrust in the north and south respectively. The northern boundary of the Lesser Himalayas (Lesser-Himalayan sequence) is defined by the Main Central Thrust and the Higher Himalayas (Greater Himalayan crystalline Complex, Tethyan Himalayan sequence) are limited by the Indus–Yarlung Zangbo River suture zone (IYS) in the north, where the boundary between the Greater Himalayan crystalline Complex and the Tethyan Himalayan sequence is defined by the South Tibetan Detachment Fault (Burg and Bouilhol, (2019)). Multiple studies (Ponraj (2019), Zheng (2017) and Yadaf (2018)) have confirmed the ongoing accumulation of strain between the Indian plate and the Eurasian plate and have found shortening/slipping rates of 15-18 mm/year.

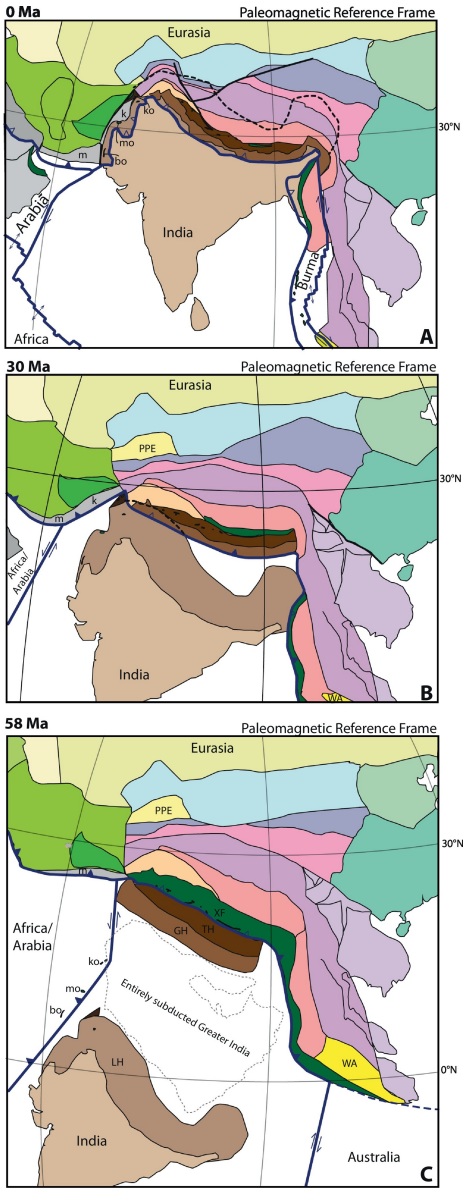

Figure 2: Kinematic restoration of deformation in the India-Asia collision zone. Note the trench parallel dragging of the Burma slab by the Indian plate going from Fig. B to Fig. A. The dotted line over Tibet in Fig. A represents the northern margin of horizontally underthrust Indian continent below Tibet as imaged by seismic tomography. In Fig. C the outline of present-day Arabia is drawn as a dotted line to provide a sense of the scale of the area of Greater India of which no accretionary record is known and that must have undergone wholesale subduction. Key to abbreviations: bo=Bela Ophiolite; GH=Greater Himalaya; k=Katawaz Basin; ko=Kabul-Altimur Ophiolite; LH=Lesser Himalaya; m=Makran; mo=Muslim Bagh Ophiolite; PPE=Proto-Pamir Embayment (see (van Hinsbergen et al., 2011a)); TH=Tethyan Himalaya; WA=Woyla Arc and West-Sumatra; XF=Xigaze Forearc Basin. Figure taken from van Hinsbergen, D.J., Lippert, P.C., Li, S., Huang, W., Advokaat, E.L. and Spakman, W., 2019. Reconstructing Greater India: Paleogeographic, kinematic, and geodynamic perspectives. Tectonophysics, 760, pp.69-94.

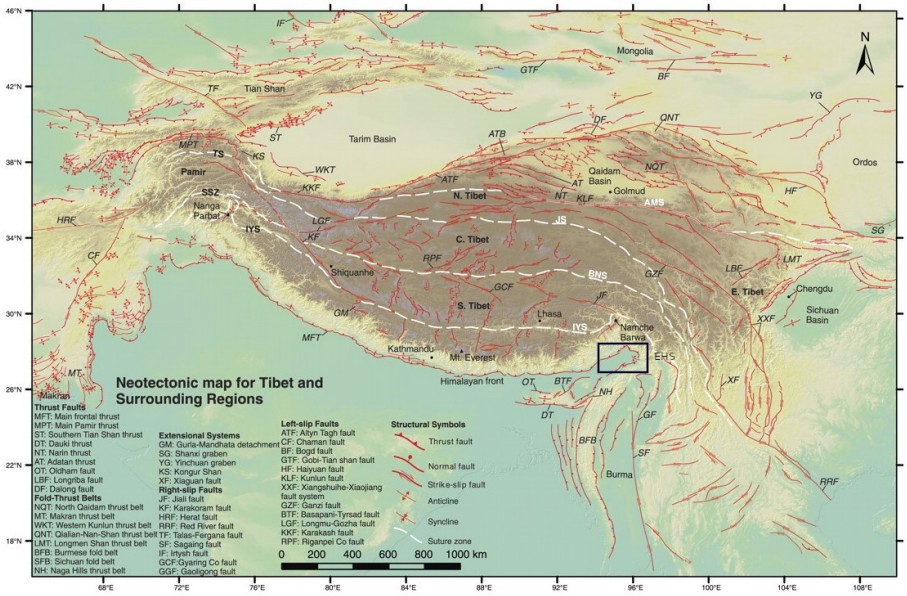

Figure 3: Neotectonic map for the Tibetan Plateau containing active to recently active faults (red) and suture zones (white) related to the Indo-Asian collision zone and surrounding regions. The Eastern Himalayan Syntaxis is highlighted by the box. Notable abbreviations are as follows; IYS = Indus-Yarlung Zangbo River suture zone, LMT = Longmen Shan Thrust belt, ATF = Altyn Tagh Fault, KLF = Kunlun Fault, XXF = Xianshuihe-Xiaojiang Faults system, KF = Karakoram Fault, EHS = Eastern Himalayan Syntaxis. Taken and adjusted from Taylor, M. and Yin, A., 2009. Active structures of the Himalayan-Tibetan orogen and their relationships to earthquake distribution, contemporary strain field, and Cenozoic volcanismActive structures on the Tibetan plateau and surrounding regions. Geosphere, 5(3), pp.199-214.

2.2 Tibetan Plateau

The Tibetan Plateau is one of the largest tectonically active regions in the world. The under-thrusting of the Indian plate and the subsequently thickening of the lower crust is reflected in the thinning of the upper crust (Styron et al., 2015). Recently Liang et al. (2013) revealed the entire plateau to undergo continuous uplifting relative to stable neighboring region to the north. The Tibetan Plateau is characterised by its many E-W striking faults which are the cause for numerous strong earthquakes in the area. Some notable faults in the Tibetan Plateau are the Longmen Shan (LMT) in the East, the Altyn Tagh fault (ATF), which marks the northern boundary of the Tibetan plateau, the Kunlun Fault (KLF), the Xianshuihe-Xiaojiang fault system (XXF) and the Karakoram fault (KF). Excluding the LMT and the KF which are a major thrust zone and a dextral strike-slip fault respectively, the majority of these faults are defined

by a sinistral strike slip movement, the XXF being the main accommodator of the clockward rotation of the Eurasian crust around the Eastern Himalayan Syntaxis (EHS).

2.3 Burma Terrane

Whereas the Indian plate converges with the Eurasian plate in a relative straightforward fashion in the North, the hyper-oblique subduction of the Indian plate beneath the Burma Terrane in the East makes for a complex geodynamic situation. Due to the obliquity of the subducting Indian plate the Burma slab is hypothesised to be subjected to (mainly) trench-parallel slab dragging, meaning it is being laterally transported by the absolute motion of the Indian plate (Spakman et al. 2018). A recent kinematic reconstruction made by van Hinsbergen (2019) supports this hypothesis (Figure 2 A,B). The Burma Terrane is separated from the Indian plate through the Naga Hills thrust belt (NH) and the Rakhine-Bangladesh Mega Thrust (RBMT) in the North-West and West, respectively. These faults are likely connected by a part of the Dauki thrust (DT). The Eastern boundary of the Burma Terrane can be found in the Sagaing fault (SF), a major north-south oriented dextral strike-slip fault stretching over 14000 km (Mon et al., 2019). In turn, the Central Basin of the Burma Terrane is separated from the Indo-Burman Ranges (IBR) by the Kabaw fault (KBF) and the Western IBR is separated from the Eastern IBR by the Churachandpur Mao fault (CMF) in the North. Both faults have NE-SW to North-South oriented strikes and the CMF is documented (Steckler (2016), Gahalaut (2013) to have a dominant dextral strike-slip component (Figure 1). Previous studies have already tried to put constrains on the strain budget of the India-Burma-Sunda system. Steckler (2016) proposes a highly oblique motion of 46 mm/yr of which 21 mm/yr of shear motion is taken up by the SF, a shortening of 13-17 mm/yr is accounted to the locked megathrust (RBMT) and the remainder of dextral motion is distributed over creep motion of the CMF (10 mm/yr) and stick-slip motion on the Kabaw Fault (5-6 mm/yr). Other authors (Gahalout (2013), Panda and Kundu (2020)) find lower total estimates of plate motion in the order of 36 mm/yr. The main difference between the estimates of Gahalout (2013) and Panda and Kundu (2020) and those found by Steckler (2016) are located around the RBMT and the CMF as the former two authors believe the remaining budget (SF not included) is concentrated on the CMF and the latter believes it to be expressed in the RBMT.

3 GPS Data

The kinematic inversion of relative motion data, and therefore the data itself, is at the core of our research. All available surface velocity estimates gathered through published geodetic studies in south-east Asia have been compiled into one large data set, from this data set all data which lie inside our model domain, from (78°, -1°) in the SW to and (114°, 36°) in the NE, will be used for inversion

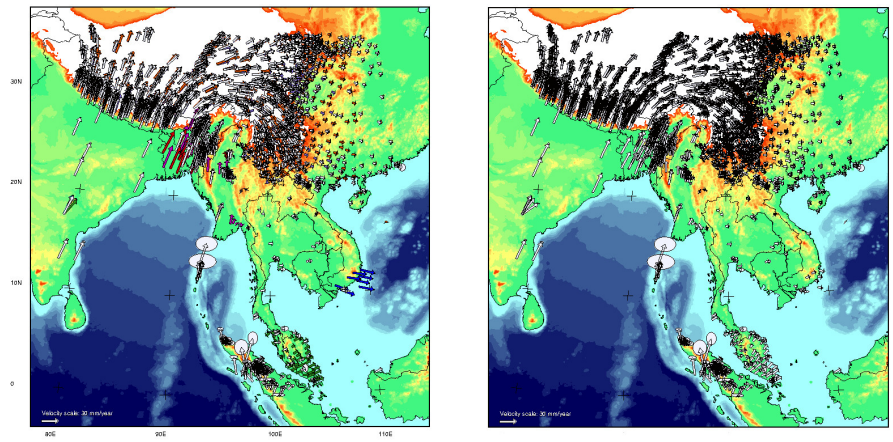

(a) (b)

Figure 4: a) the 9 data sets used in this research, different colors of arrows correspond to different data sets (and different reference frames); White = Kreemer et al. (2014), red = Steckler (2016), purple = Pan (2018), pink = Mallick (2019), blue = Yadav (2018), orange = Zheng (2017), yellow = Ponraj (2019), green = Mustafar (2017), dark blue = Nguyen (2020) b) All data rotated into the Kreemer Eurasia reference frame, Euler poles can be found in Table 1

3.1 Data acquisition

For our initial setup 2914 data points from measurements of 1371 continuous and campaign-mode GPS stations with a time interval ranging between 2 and 25 years have been gathered. The data has to meet specific requirements to be of use in our research. Six key parameters are required as input for a kinematic experiment; longitude, latitude, longitudinal and latitudinal velocity and the standard deviation of the east-north velocity components. Preferrably, the data are also labeled with a four character station code and an east-north error correlation, the latter, if not present, will be set to zero.

The Kreemer et al. (2014), hereafter Kreemer14, data set will function as a reference data set as it combines all processed GPS data available through other published papers up to 2014 with up to 1400 data points located in our research area. The Kreemer14 data set shows a high density of data points across various regions in our reference frame, specifically across the Himalayas, Sumatra and the NE part of India. With the addition of 8 recently published data sets, described below, we aim to supplement the area's suffering from low density data coverage (Figure 4a). The additional data sets will be crosschecked with the Kreemer14 data set to reduce the possibility of duplicated data. Besides Kreemer14 two relatively large recent data sets have been published in papers by Zheng (2017) and Pan (2018) with 729 and 657 data points respectively.

The Zheng and Pan data sets both add abundant data points in China; on the Eurasian plate and the Yangtze plate, while the latter also adds several data points on the relatively poorly covered Tibetan plateau. The remaining data sets consist of significantly less data points, containing anywhere from 3 to 60 data points. (Mustafar et al., 2017, Mallick et al., 2019, Steckler et al., 2016, Ponraj et al., 2019 Yadav et al.,2018, Nguyen et al., 2020). The Mallick and Steckler data sets both add data points in Bangladesh and Burma (Myanmar) and the remaining data sets add some data points in Malaysia, Thailand, India, Vietnam, China and the Himalayas. Unfortunately, large areas still remain low on data density.

Globally, GPS motions can be established in different velocity reference frames. Most tectonic plates hosting GPS stations rely on a velocity reference frame which measures motion with respect to their own plate (Pacific fixed, Eurasia fixed etc.) as well as a global velocity reference frame (IGS) that underly the global geodetic ITRF frame (e.g. Collilieux et al. 2014). We adopt the Eurasian frame of our base data set Kreemer14.

The other data sets may have been published in different reference frames (e.g. "blue" south Vietnam network in Fig. 4a) or may still have a small overall network rotation relative to Kreemer14 which may result from using a different set of IGS reference stations. To translate multiple different velocity reference frames into a singular network we will first solve for the relative network rotations only, the rotated network can be observed in figure 4b. Details of the method behind this rotation and a table containing all obtained Euler poles and rotations can be found in chapter 4.1.1 and 5.2 respectively.

After rotating all networks in the Kreemer14 frame still several data point locations are found with data from multiple data campaigns, of which two show greatly diverging motions as compared to the other vectors and spatial trends in the overall surrounding data. We hypothesize this could be due to displacement linked to a local landslide or an earthquake. The concerned area has been subject to multiple earthquakes in 2008 near the coordinates of both points (United States Geological Survey), since the data campaign containing these two measurements was taken in the 2005-2008 window this seems like a valid possibility. Both data points are clear outliers which are deemed not likely to represent the general motion of their respective area and therefore have been removed.

4 Methods

4.1 The Spakman-Nyst method

We make use of the Tetra program, which is developed and written by W. Spakman. This program applies the method of Spakman and Nyst (2002) for a purely kinematic analysis of relative motion data, here, of the surface deformation field of the Burma platelet and its surrounding region. The method does not require any assumptions about the dynamics causing the deformation or the rheology

of the crust and leads to estimates of the strain- and rotation-rate fields, surface fault creep/slip, and relative network rotations. The method is briefly described in the following section.

4.1.1 The observation equation

A surface deformation field can be estimated from the relative motions Δv_{ij} considering any integration path Ł$_{ij}$ of arbitrary geometry connecting any two stations i and j. For each i -j site pair the S-N method is based on the following observation equation for the relative motion Δv_{ij}:

$$\Delta \mathbf{v}_{ij} = \sum_{l=1}^{K+1} \int_{L_{ij}^{l}} \nabla \mathbf{v}(\mathbf{r}) \cdot d\mathbf{r} + \sum_{k=1}^{K} \alpha_k \mathbf{f}_k(r_{ij}^{k}) \tag{1}$$

The first part of the right-hand side deals with continuous surface flow along an integration path Ł$_{ij}$. Since Δv_{ij} can be discontinuous at faults this part has been divided into l segments as to shape multiple continuous surface flow fields separated by K faults. The unknown velocity gradient tensor field is described by $\nabla \mathbf{v}(\mathbf{r})$. The second part of the right-hand side incorporates fault motion into the equation where $\mathbf{f}_k$ is the unknown fault slip rate and $\alpha_k = -1$ or $+1$ depending on the fault orientation with respect to the direction of integration path Ł$_{ij}$.

To account for relative rotation between network solutions a final term in the form of $\mathbf{\Omega}_j \times r_j - \mathbf{\Omega}_i \times r_i$, where $\mathbf{\Omega}_j$ and $\mathbf{\Omega}_i$ represent the Euler rotation vector relative to the reference data set for the observation network to which stations j and i belong, respectively, can be added to equation 1. Altogether this observation equation gives a complete description of the relative crustal motion data Δv_{ij} and is purely linear in the unknown quantities $(\nabla \mathbf{v}(\mathbf{r}), \mathbf{f}_k, \mathbf{\Omega}_j)$ and, as no theoretical approximations are made, the equation is exact.

4.1.2 The forward & inverse problems

The study region is subdivided by N model nodes connected by triangulation, depending on the local data density the spatial density of nodes can be varied. The N nodes do not need to coincide with observation sites. The only restriction is that triangles may not intersect with faults that are implemented in the model. Fault segments need to follow edges of the triangles that parameterize the model domain. This puts a priori constraints on the triangulation design of the model domain.

If we have a set of P data point positions with known relative motions these positions yield (at least) $P(P-1)/2$ vector equations (1) along paths L_{ij} for all possible combinations of sites i and j. The velocity gradient field $\nabla \mathbf{v}(\mathbf{r})$ is parameterized by assuming linear variation of the tensor components in a triangular subdomain of the study region, this parameterization allows for quadratic velocity variation within triangles and continuity of $\nabla \mathbf{v}$ across triangle edges. The fault slip rate $\mathbf{f}_k$ is implemented as a linear variation of

fault slip between the segment endpoints rather than by assuming constant slip rate on fault segments (k), as originally stated in Spakman and Nyst (2002). The coupling between the vector equations is provided by the crisscrossing of integration paths that sample the triangulated model domain. Solving this coupled set of integral equations is the inverse problem.

The coupled set of integral equations can be written in matrix-vector form according to $\hat{\mathbf{A}}\mathbf{m} = \hat{\mathbf{d}}$, where $\hat{\mathbf{A}}$ contains the observation matrix, $\mathbf{m}$ represents the model parameters and $\hat{\mathbf{d}}$ is the vector that combines all relative motion between station pairs. The minimum length of $\hat{\mathbf{d}}$ is equal to $P(P-1)/2$ but can be extended by defining extra integration paths L_{ij} between station pairs depending on the modellers wishes. This is done to assure internal consistency between the velocity gradient field and fault motion in constituting the total deformation field and also to put constraints on the null space of the inverse problem (when adding closed integration paths $L_{ij} - L_{ji}$). The latter are explicitly included as circle-paths around model nodes and closed paths inside each triangle following the triangle edges. This forces the velocity gradient solution $\mathbf{v}(\mathbf{r})$ to be curl-free which characterizes a deformation field (Spakman and Nyst 2002).

Given a triangulation of the model domain, we still may need to deal with the possible inconsistency in the equation set due data errors, with non-uniqueness, and with possible ill-conditioning of the matrix. To this end we use a regularized inversion scheme which selects a solution that fits the data in a least squares sense while also minimizing the model norm. The object function to be minimized can be stated as followed:

$$\begin{aligned}\mathbf{\Phi}(\mathbf{m}) =&(\mathbf{Am} - \hat{\mathbf{d}})^{\mathbf{T}}\mathbf{C_d^{-1}}(\mathbf{Am} - \hat{\mathbf{d}}) \\ &+ \alpha^{\mathbf{2}}\mathbf{m^T D^T Dm}\end{aligned} \tag{2}$$

Where $\mathbf{C_d}$ denotes the data covariance matrix, the $\mathbf{D}$ represents a damping operator and α controls the trade of between minimizing the weighed model norm and fitting the data. Tetra allows for amplitude damping as well as 1^{st} and 2^{nd} derivative damping transforming equation 2 into:

$$\begin{aligned}\Phi(\mathbf{m}) =&(\mathbf{Am} - \hat{\mathbf{d}})^{T}\mathbf{C}_d^{-1}(\mathbf{Am} - \hat{\mathbf{d}}) \\ &+ \alpha_0^2\mathbf{m}^T\mathbf{m} + \alpha_1^2\mathbf{m}^T\mathbf{D}_1^T\mathbf{D}_1\mathbf{m} \\ &+ \alpha_2^2\mathbf{m}^T\mathbf{D}_2^T\mathbf{D}_2\mathbf{m}\end{aligned} \tag{3}$$

Since we choose to work with amplitude damping only, the object function Φ as well as the model $\mathbf{m}$ that minimizes Φ effectively reduces to:

$$\mathbf{\Phi}(\mathbf{m}) = (\mathbf{Am} - \hat{\mathbf{d}})^{\mathbf{T}}\mathbf{C_d^{-1}}(\mathbf{Am} - \hat{\mathbf{d}}) + \alpha_{\mathbf{a}}^{\mathbf{2}}\mathbf{m^T m} \tag{4}$$

$$\mathbf{m} = (\mathbf{A^T C_d^{-1} A} + \alpha_{\mathbf{a}}^{\mathbf{2}}\mathbf{I})\mathbf{A^T C_d^{-1}}\hat{\mathbf{d}} \tag{5}$$

Where $\mathbf{I}$ stands for the amplitude damping identity matrix.

5 Experiments

We have inverted our data for 4 different model representations and fitted the data on the basis of a 1 sigma data error. First we will look into the role of faults within our research area. Model 1 is solely solved for fault slip, this implies the assumption that a crustal deformation field is only controlled by motion/creep on faults, which are not locked at the surface and are allowed to slip freely (i.e. assume rigid motion of large crustal blocks). Model 2 will add rotation rate as a parameter at nodes, allowing crustal blocks to rotate, resulting in a model that mimics block-fault models. Then we will explore the effect of the absence of faults slip in model 3, which assumes faults are locked at the surface and relies on continuous deformation. Finally, in model 4 we will also allow for fault slip combining all available model parameters. We will primarily focus on the Himalayan mountain range, the Sagaing fault and the upper part of the Burma platelet. We will not go into detail about the southeastern part of the model since this is a very poorly constrained part of the model while also being of little relevance to our research question.

5.1 Model parameterization & analysis tools

To parameterize the study area we make use of a Delaunay triangulation which is constructed through a divide and conquer method (Shewchuk, 1996). We let triangle size vary based on location within the model (boundary vs center) and station density. The triangulation has been improved iteratively through multiple inversion for optimizing our solution in the sense that the data are properly fitted. This results in triangle sides spanning from 1 degree at the model center, where we have high density data areas, up to 3 degrees along the boundary and at locations without data coverage, like the Bay of Bengal or the Andaman sea. A convex shaped model is chosen to keep site connecting great circles L_{ij} contained in the model.

In total the model has been parameterized by 416 triangles which are spanned by 224 nodes and 25 fault segments (Figure 5). 26 out of 224 nodes are doubled to function as fault notes, this is done in order to allow the velocity gradient field to be discontinuous across faults.The vast majority of nodes, with the exception of fault nodes, are placed on data points for maximum data utilisation.

The amount of model parameters is determined through the amount of velocity gradient tensor components (VG components $\times$ VG nodes), the inclusion of rotation vector components (3 $\times$ number of data sets to be rotated) and fault slip components (2 $\times$ number of FS nodes). Our models have increasing amounts of model parameters depending on the inclusion/exclusion of the aforementioned options.

To account for plate boundaries and major faults, nearby triangle vertices have moved to coincide with the fault lines basically defining fault segments. While the majority of plate boundaries locations are derived from Argus (2011) small adjustments have been made based on literature and motion data, specifically concerning the EHS as this is a key location for correctly interpreting the

geodynamics of the Burma platelet. The boundary between the northern part of the Indian plate and the Eurasian plate is taken from Argus and placed along the MFT, the Burma plate however will be parameterized differently. We take the initial Burma platelet from Argus but instead of ending in the Andaman sea we will let it follow the RBMT in the West (Mallick et al.,2019) until the NH connects it to the MFT (much like Khan et al., 2017). The Eastern boundary of the Burma plate will be taken along the SF. The boundaries between Eurasia-Sunda and Eurasia-Yangtze roughly correspond to how they have been defined in Argus, however, due to a lack of available data in both respective areas we will not solve for fault creep along these boundaries.

We assume the Indian plate to be rigid, in the large unsampled regions such as the Bay of Bengal. To enforce rigid behavior 57 synthetic data points have been added of which 49 are given the Euler velocity of the Indian plate. The remaining 8 data points are located on the Assam (2) and Shillong (6) block and will be given their respective Euler velocity (Vernant et al., 2014), all relative to the Kreemer14 reference frame.

Finally we impose several boundary conditions on the model; Euler velocities will be imposed on boundary nodes and segments corresponding to their respective tectonic plates, furthermore strain rate along the boundary will be damped to (near) zero to suppress deformation and to support rigid plate rotation.

To analyse the results of our inversion we will be looking primarily at χ_v^2, the resolution and the covariance to determine an acceptable solution. χ_v^2 will be defined as in e.g. (Bos et al., 2003):

$$\chi_v^2 = \frac{1}{v} \sum_{i=1}^{N} \frac{{e_i}^2}{{\sigma_i}^2} \tag{6}$$

Where $v = N - M$ is the degrees of freedom of the model with N and M being the number of data equations and the number of model parameters respectively. σ_i^2 is the 1σ data variance and $e_i = d_i^{obs} - d_i^{pre}$ defines the prediction error of the model. The expressions for model covariance and resolution are taken from Spakman and Nyst (2002):

$$\mathbf{C}_m = \left(\mathbf{A}^T\mathbf{A} + {\alpha_0}^2\mathbf{I} + {\alpha_1}^2{\mathbf{D}_1}^T\mathbf{D}_1 + {\alpha_2}^2{\mathbf{D}_2}^T\mathbf{D}_2\right)^{-1} \tag{7}$$

$$\mathbf{R} = \mathbf{C}_m\mathbf{A}^T\mathbf{A} \tag{8}$$

Ideally, χ_v^2 should be around 1. It can depart from 1 if the published GPS vector errors are incorrect representations of the (unknown) actual errors, if the model is under- or overparameterized, or if the regularization/damping is too strong. Given these uncertainties, we aim for a model with a χ_v^2 of 10 or lower and, importantly, try to understand any deviation from 1. Furthermore, the standard deviation (c-av) will have to be substantially smaller than the solution amplitudes (s-av) and the model resolution has to be above 0.5, but preferable close to 1, for our solution to be acceptable.

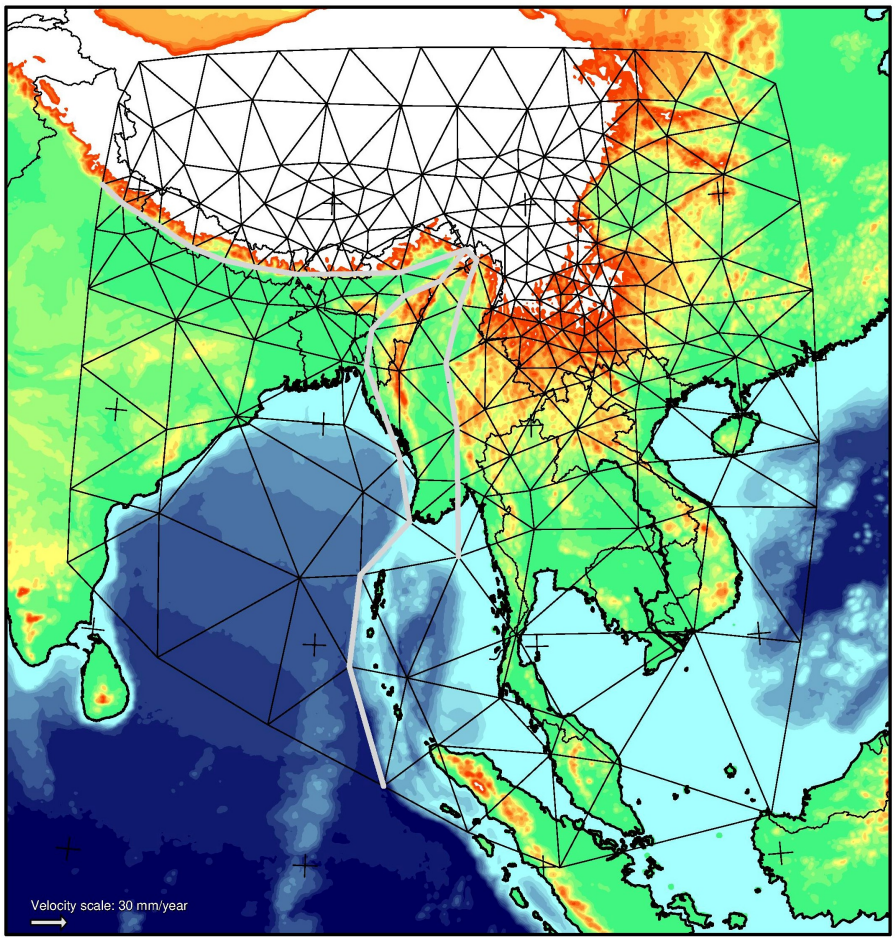

Figure 5: Final model parameterization; 416 triangles spanned by 224 velocity gradient nodes and 26 fault slip nodes

Another important analysis tool is the velocity prediction field that is a posteriori computed from the model. We perform this analysis after correcting for network rotations relative to the reference network. From the solution of the inverse problem a prediction of the velocity field on a (regular) synthetic grid can be performed according to:

$$\mathbf{d}^{pred} = \mathbf{A}^{pred}\tilde{\mathbf{p}} \tag{9}$$

Each grid point is seen as a data point with an unknown velocity and will be connected to all data sites through integration paths for which the r.h.s. of eq. 1 is determined leading to a matrix $\mathbf{A}^{pred}$ that assembles all the combinations of synthetic sites and data sites. The model vector $\tilde{p}$ is the actual solution of the inverse problem that was obtained from the GPS motion data. $\mathbf{d}^{pred}$ thus constitutes all the velocity differences between the GPS sites and the synthetic sites. We next calculate the velocity prediction at synthetic site i as follows

$$\mathbf{v}_i^{pred} = \frac{1}{M}\sum_{k=1}^{M}\mathbf{v}_k^{GPS} + \mathbf{d}_{ik}^{pred} \tag{10}$$

where $\mathbf{d}_{ik}^{pred}$ is the relative velocity between data site k, with velocity $\mathbf{v}_k^{GPS}$, and synthetic site i. Errors in the model solution $\tilde{p}$ cause scatter in $\mathbf{v}_i^{pred}$ Which is represented by a 1σ confidence ellipse in plots of the the prediction vectors. This prediction can give us insight into the validity of our models (i.e. large error ellipses might be a sign of a poor solution in the respective area).

5.2 Relative Network rotations

As mentioned in chapter 3.1 we will first rotate all obtained data sets into the reference frame of Kreemer after which all vectors at single sites are averaged into 1 vector and merged with the reference network. All obtained Euler poles w.r.t. Kreemer can be observed in Table 1.

Dataset	Longitude	Latitude	Rotation (deg/Myr)	Error (deg/Myr)	Error (%)
Steckler	-69.565	-14.051	0.254070	0.016420	6.5
Pan	-95.537	-27.101	0.060700	0.001000	1.6
Mallick	-75.814	-21.330	0.355650	0.012920	3.6
Yadav	-106.920	-17.569	0.065240	0.008880	13.6
Zheng	-129.932	-28.009	0.021100	0.000980	4.6
Ponraj	-91.586	-27.449	0.404130	0.098500	24.4
Mustafar	179.434	27.315	0.032140	0.002620	8.2
Nguyen	113.491	23.669	0.708990	0.102330	14.4

Table 1: Computed Euler poles and their errors after 4 iterations

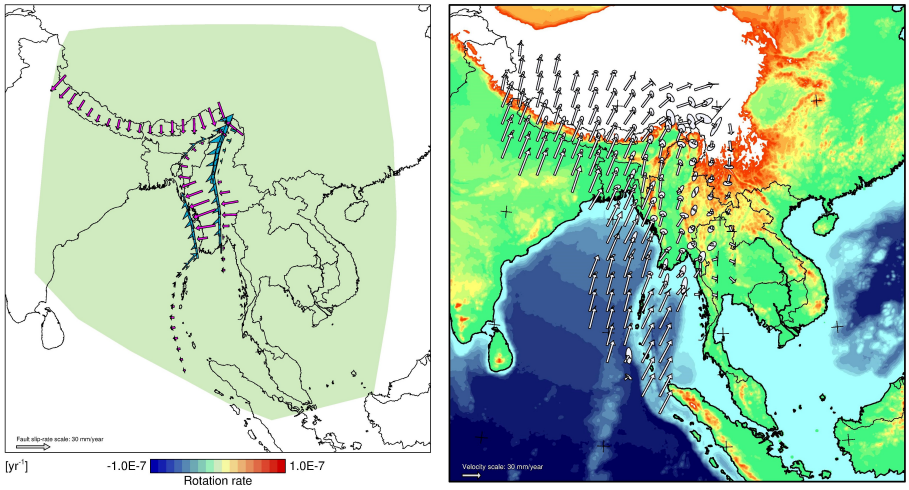

(a) fault slip

(b) velocity prediction field

Figure 6: Results of an inversion after solving for pure fault slip. a) The colour of the arrows correspond to fault type; for parallel motion yellow=sinistral, blue=dextral and for normal motion pink=thrust and blue=normal b) The velocity prediction shows significant error ellipses in key locations like the EHS

5.3 Model 1: fault slip

As previously stated we will not consider all major faults , we have chosen to ignore several due to lack of data coverage in the respective areas, minor faults have been ignored all together for the sake of simplicity. The faults are represented by 26 fault slip nodes, each node is composed of a fault normal and a fault parallel component, leading to a total of 52 fault slip parameters. Since our model relies only on fault slip our values (figure 6a) will be estimates of the total convergence/shortening rate. We find a high χ_v^2 value of 79.0 indicating a poor fit. Furthermore, we also observe a general CW rotation around the EHS in our velocity prediction field. However, the high concentration of error ellipses accompanying most predicted velocities in this respective area once again implies a poor solution (figure 6b).

5.3.1 MFT

The dominant fault motion shows to be a combination of dextral slip dip faults and thrust faults and although this general trend does comply with literature the magnitude of our slip values falls short in some areas. Our model shows a shortening rate of 7-18 mm/yr along the MFT with average shortening rates of 13 mm/yr and 17 mm/yr in the west and east respectively. Besides our central Himalayan shortening rate of 7-9.4 mm/yr, which seems to be on the low side, our shortening rates are in the same order of magnitude when compared

to Zheng who found 15 mm/yr on all their profiles along the MFT and with Yadav and Ponraj who found a rate of 18 mm/yr and 17 mm/yr respectively. Our shortening rate in the eastern Himalayas is in agreement with both Yadav and Ponraj as well as those of Banerjee (2008).

5.3.2 NH

Besides a dextral slip component ranging from 5 mm/yr in the west up to 10 mm/yr in the middle we also find a normal component of fault slip of 4 mm/yr in the west which declines eastward before rising up to 7.7 mm/yr near the EHS. Vernent (2014) also found indications of spatially diverging convergence which increases from 1–2 mm/yr in the west, south of the Mikir Hills, to more than 5 mm/yr in the east based on the Euler pole rotations of the Assam block (figure 1) and the Burma plate with respect to the Indian plate. We speculate that the larger normal component in the west may be related to the DT which is estimated to accomodate up to 9 mm/yr of fault normal slip while the dextral component is in line with the slip corresponding to the NH found in Panda, Kundu & Santosh (2018).

5.3.3 RBMT

The Rakhine-Bangladesh megathrust is estimated to accommodate a convergence spatially varying from 12 to 24 mm/yr with a minimal strike slip component(Mallick et al., 2019). However, Mallick states they expect their results to show more strike slip when taking the RBMT more accurately. We find spatially varying converging rates of 5 to 16 mm/yr and a dextral strike slip component of up to 19 mm/yr in the south and 8 mm/yr in the north. The former being on the low side and the later being significantly higher.

5.3.4 SF

The SF show high dextral slip increasing from 9.4 mm/yr in the south towards 28.3 mm/yr in the North. The upper limit of 28.3 mm/yr is significantly higher than that of most other studies (Steckler et al., 2016, Mallick et al., 2019). In addition we also find a relatively strong fault normal component along the SF of up to 14.6 mm/yr in the south and a smaller component of 1-5.1 mm/yr in the north, besides Mallick who found a small fault normal component of 1-5mm/yr this component has not been documented in literature. When we compare our obtained fault slip results to geologic/geodetic studies we do find similarities, however, we also know our research area to be heavily subjected to earthquakes, making it unlikely for all motion to be accommodated by aseismic, freely slipping faults. Furthermore, taking in mind the poor data fit and velocity prediction we find model 1 fails to correctly describe the GPS data.

5.4 Model 2: block fault

We aim to mimic a block fault model with the addition of rotation rate as a parameter at nodes model 2 will consist of 416 triangles spanned by 250 nodes and 302 model parameters. We observe a reasonable decrease in the χ_v^2 value (=60.2), unfortunately this value still represents a poor data fit. Despite a poor data fit the model does have a solid resolution (r-av=0.9810) and covariance (c-av=0.9543E-5).

5.4.1 Fault slip

Figure 7a shows the fault slip components of model 2. We can observe the same general trend we saw in model 1 but with some distinctions; An increase in sinistral strike slip motion along the Eastern Himalayas, a strong decrease in dextral slip motion accompanied with some normal fault slip along the NH, a relatively strong increase in the fault normal component of the RBMT (up to 25.6 mm/yr) and a reduced normal component with a thrusting motion instead of a normal motion in the north combined with less dextral strike slip along the SF. Our findings for the RBMT and the SF are similar to those found in Vernent (2014) and Mallick (2019). The decrease in dextral slip motion along the NH however does not find support in literature.

5.4.2 Rotation rate

We observe a dominant CW rotation rate of the Burma plate and the Assam block, as well as the parts of Eurasia adjacent to the Eastern Himalayas. This rotation rate reaches up to 1 °/myr in the south, 5.7 °/myr in the north of Burma and 2.35 °/myr in Eurasia and is in compliance with general rotation motion of this area as taken from paleomagnetic data (Westerweel et al., 2009, Otofuji et al., 2010). A small counterclockwise (CCW) rotation rate (0.4 °/my) is observed in the remaining Tibetan Plateau in the north of our model and east of Burma. Otofuji (2010) found up to 1.7 °/my of clockwise (CW) motion centered around Burma and up to 2.25 °/my of CCW motion adjacent to Burma, which is slightly smaller and larger than our respective CW and CCW rotation rates. Nonetheless both results fall into the same order of magnitude. In contrast to Otofuji we do seem to find a small CW rotational movement in the eastern part of the Qaidam Block (top right in our model) which corresponds with paleomagnetic data although in much smaller magnitude (Otofuji, 2010).

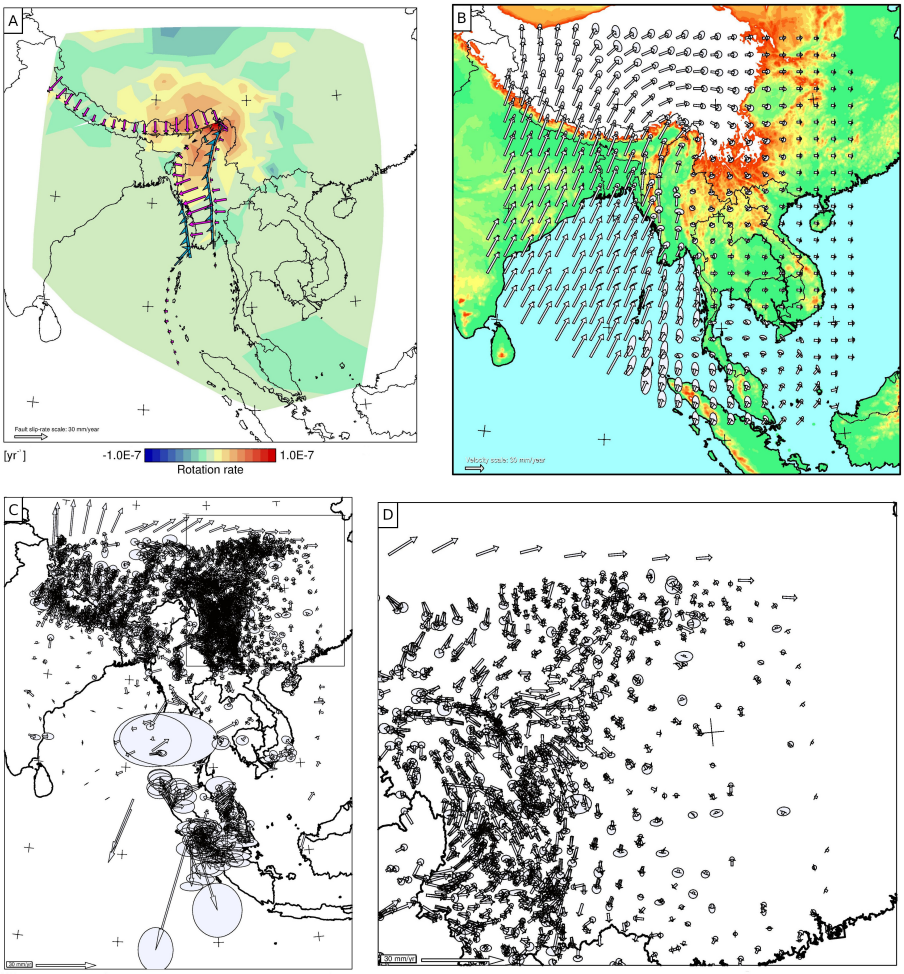

Figure 7: Results of an inversion mimicking a block fault model. A) fault slip, the background colour is related to rotation rate; red = CW and blue = CCW, see figure 4 for more details. B) Velocity prediction field, smaller error ellipses can be observed in key locations with respect to model 1. C) Misfit vectors of the entire model, the black box shows the location of D).

5.4.3 Velocity field prediction

In figure 7b we notice the velocity field prediction has improved with respect to the velocity field prediction of model 1. We can observe the general CW rotation rate around the EHS with smaller error ellipses then before, however, there are still plenty of relatively large error ellipses observed, specifically around Sumatra, Burma and the northern Tibetan Plateau.

5.4.4 Misfit vectors

When we look at our misfit vectors (figure 7c/7d) we can observe multiple large misfit vectors, especially on the northern boundary and near Indonesia, explaining our rather high χ_v^2 value. The majority of these large misfit vectors can be linked to our data set covering Sumatra and the Andaman islands and synthetic data in the north-west and the south. The former having exceptionally large error ellipses, indicating the data to be of questionable quality at best. This could be related to tectonic structures in this area not included in our model, like the Sumatra Fault System, seeing as many stations are located at both sides of this fault. The center and eastern part of our model is relatively well described as is reflected in the small misfit vectors which fall inside their error ellipses (figure 7d).

While Model 2 is definitely an improvement over model 1 the data fit is still too poor for model 2 to correctly explain the data. However, this does not come unexpected as it is unlikely for all faults to be slipping silently. Still, it does show us how rigid block motion maps on the faults if there would be no internal block deformation.

5.5 Model 3: continuous deformation

Since we do not solve for fault slip, this model is parameterized by 416 triangles spanned by 224 nodes and 896 model parameters (4×224). Model 3 has a significantly better fit then the previous models, with a χ^2 value of 12.7. Figure 8 show the strain rate, rotation rate, velocity prediction field and the model covariance of all four components of the velocity gradient tensor. Low standard deviation is found in all four components, with an average standard deviation of 0.2146E-9. When compared to an average solution amplitude of 0.1409E-7 and combined with an average resolution of 0.911 this makes for an acceptable solution.

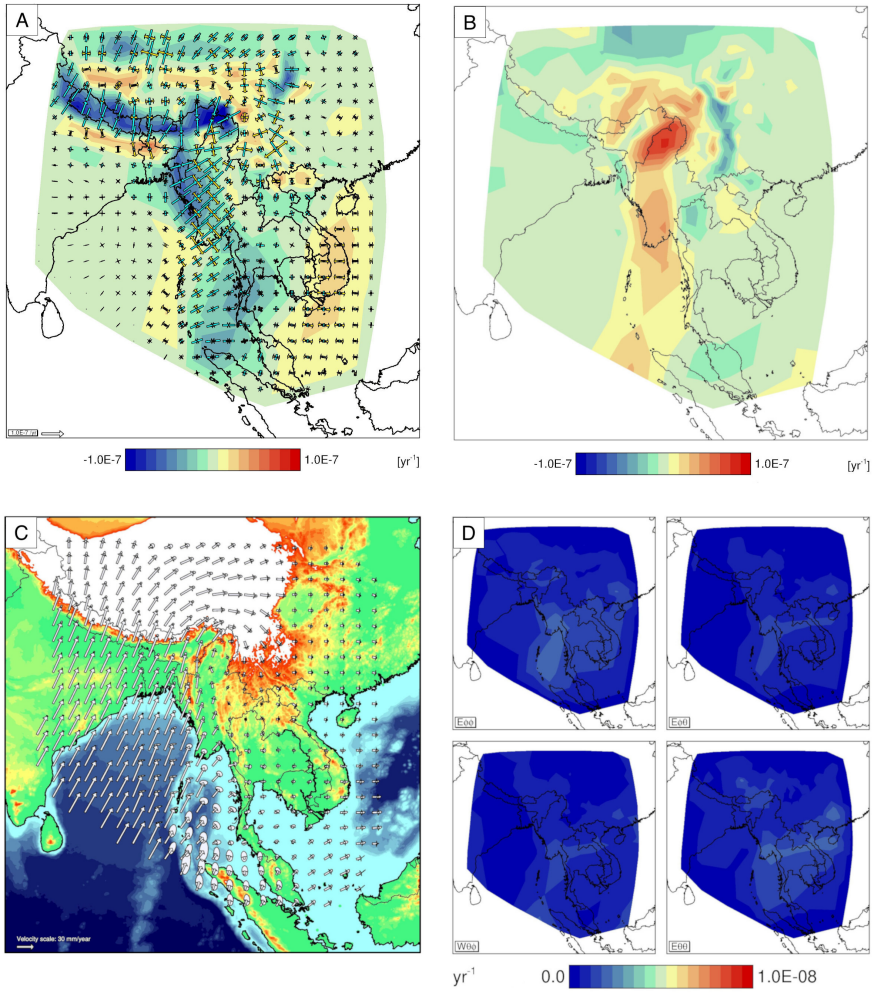

Figure 8: Results of an inversion mimicking continuous deformation. A) Strain rate with contractional strain expressed in blue arrows and extensional strain expressed in yellow arrows. The size of the arrows corresponds to the magnitude of the strain rate as given in the bottom left corner. B) Rotation rate; A dominant CW rotation rate in Burma and along the EHS combined with a stronger CCW rotation rate north and east of Burma can be observed. C) The velocity prediction shows significant improvement in important areas surrounding Burma even though it is still lacking in southern Burma. D) Model covariance of all four components of the velocity gradient tensor with a low standard deviation in all components.

5.5.1 Strain rate

We previously mentioned our assumption of India acting as a rigid plate, we can observe the addition of the synthetic data works as intended as it does indeed result in low strain rates in the Indian tectonic plate. However, a small extensional component of strain rate is still found south of the thrust front, using more synthetic data may suppress this. The Yangtze plate also shows a strain rate close to zero, implying it to be rigid as well. We find a contractional strain rate ranging from 0.5E-7/y up to 1E-7/y along the MFT with a peak in the EHS. This is in accordance with Zheng (2017) and Pan (2018) who found contractional strain in the order of 1E-7/y. Ponraj (2019) suggested a total accumulation of 61E-6 of strain resulting in a magnitude 8 earthquake every 600 years, this agrees with our findings as it translates to a strain rate of 1.0E-7/y. We observe low net strain rates all across the SF, which is to be expected due to the even presence of both contractional and extensional strain which is needed for the strike slip movement for which the SF is known. Along the NH we find extensional strain rates similarly to Pan. Much like Zheng (2017), the western boundary of the Burma plate is defined by contraction with the addition of an extensional component in the South. The center of the Burma plate shows contraction with a small strike slip component, corresponding to the hypothesised dextral component of the Kabaw fault (Wang et al., 2014). The Tibetan Plateau shows a contractional strain rate as well as an extensional strain rate in the north and the center respectively. Note the location and strike of this contractional strain rate field corresponds to the LMT in the North-East of our model. When compared to the results of Pan (2018) we can observe similar distributions of strain rate along the MFT, NH,LMT and the central Tibetan Plateau, although our solution shows a slightly larger contractional strain rate, especially in the north.

5.5.2 Rotation rate and velocity prediction

We observe a similar rotation rate for our model center when compared to the center of model 2. This model however, shows a larger CW rotation rate in the Southern part of the Burma plate and a larger CCW rotation rate east of Burma, the latter now being more in range with Otofuji (2010). The small CW rotation zone near the Quaidam block from model 2 also seems to have become smaller, making our finding more in line with Otofuji and less with paleomagnetic data.

The velocity prediction has improved significantly when compared to model 2. Most error ellipses have reduced in size with a notable amount and the only region still displaying large error ellipses being the poorly covered southern part of the Burma plate.

Solving for continuous deformation does result in generally reasonable strain rates and rotation rates. However, the presence of several active, partially aseismic faults is suggested (Gahalaut et al., 2013), making the scenario of only continuous deformation an unprobable one.

5.6 Model 4: fault slip and continuous deformation

Our final model is parameterized similarly to model 3 but with the addition of 2 X 26 fault slip parameters leading to a total of 948 model parameters. With a χ^2 of 10.7 this model has the best data fit out of all our models. Although this model has the lowest χ^2 value out of all our models it is still significantly larger than the desired value of 1. A reason for this deviation from 1 can possibly be found in wrongly appointed error ellipses linked to each GPS measurement as well as the inclusion of the poorly defined Indonesian islands in our model. Adjusting the parameterization to not include the southern part of our model could therefore possibly lower the χ^2 value. We observe relatively large standard deviation for the longitudinal strain rate components (ϕ/ϕ) of the Sumatra-Andaman fault system and around the Assam block/EHS, but to a lesser extent.The latitudinal strain rate standard deviation(θ/θ) of the latter does show large standard deviation again. The highest rotation rate (θ/ϕ) standard deviation is also found in the same two regions.

5.6.1 fault slip

When compared to model 1 a significant decrease in the amount of fault slip can be noted, this is roughly compensated by the amount of strain accumulating along all faults to be released in the form of earthquakes. The most notable difference in fault slip can be observed along the MFT, where model 4 suggests there to be nearly any fault slip at all and instead finds a large contractional strain rate. Other major faults show a smaller but still notable reduction in their fault slip components, with the SF only releasing up to 13 mm/yr through fault slip.

5.6.2 strain rate

We observe a similar strain rate distribution when compared to model 3 but with a general increase in magnitude along the MFT, where we find values of up to 2.0E-7/y. We find a decrease in magnitude of strain rate in the center of Burma and in the Tibetan plateau although this decrease appears to be proportional to the increase in fault slip. Furthermore we do not find significant extensional strain rate in the Northern part of the Indian plate indicating a more rigid Indian plate.

5.6.3 rotation rate

Figure 9a shows a large increase in rotation rate in the southern part of the Burma plate resulting in an almost evenly rotated Burma plate. We also find a relatively large CCW rotation rate for the Assam block (NE India), this rotation rate comes as a surprise and finds no back up in literature, in fact according to Vernent (2014) it is even suggested that the Assam block has a CW rotation rate (with respect to India). The general direction of rotation for the Tibetan Plateau and the region surrounding the EHS do look to be in line with Otofuji

and thus in contrast with paleomagnetic data in some places (e.g. region "N" described in Otofuji located at 35°N, 103°E).

We have tried improving model 4 by damping the poorly defined Sumatra-Andaman region and the NH, which we suspect to have heavy influence on the rotation of the Assam block. The results show an overall decrease in rotation rate and most importantly a significant decrease in CCW rotation rate in the Assam block (Figure 9b) while also significantly lowering the standard deviation in the respective areas, backing our assumption (Figure 10c/d). Even though this is an improvement over model 4 without damping we still believe our final model does not describe the motion of the Assam block well enough, Kayal suggest the Koipili fault to be the main driver behind the CW rotation rate of the Assam block (Kayal et al., 2012). Implementing this fault in future research could help improve our model. We find Model 4, after damping, to be a good enough fit to the data in all other places while also retaining good standard deviations and reasonable resolution.

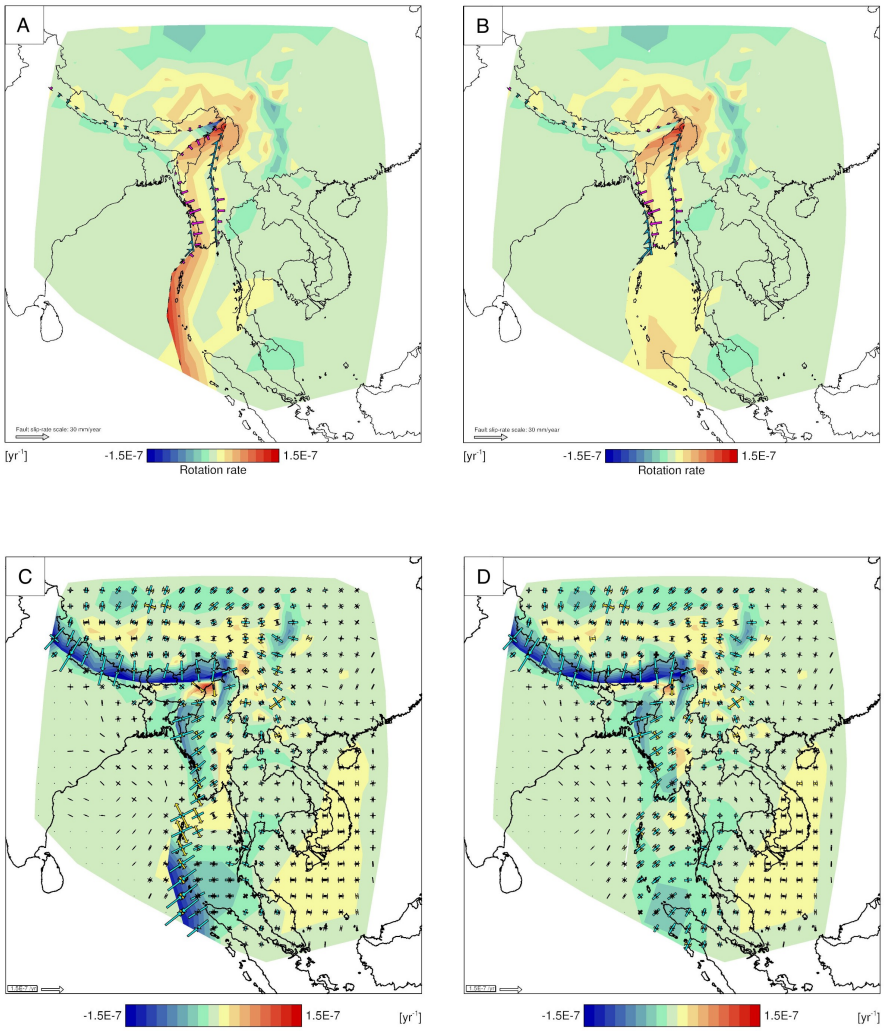

Figure 9: Results of an inversion including both fault slip and continuous deformation (1). A) Fault slip and rotation rate before damping. B) Fault slip and rotation rate after damping, an overall decrease in rotation rate and most importantly a significant decrease in CCW rotation rate in the Assam block can be noticed. C) Strain rate before damping D) Strain rate after damping; significant decrease in strain rate along the Andaman fault system and a smaller extensional strain rate in the Assam block/EHS.

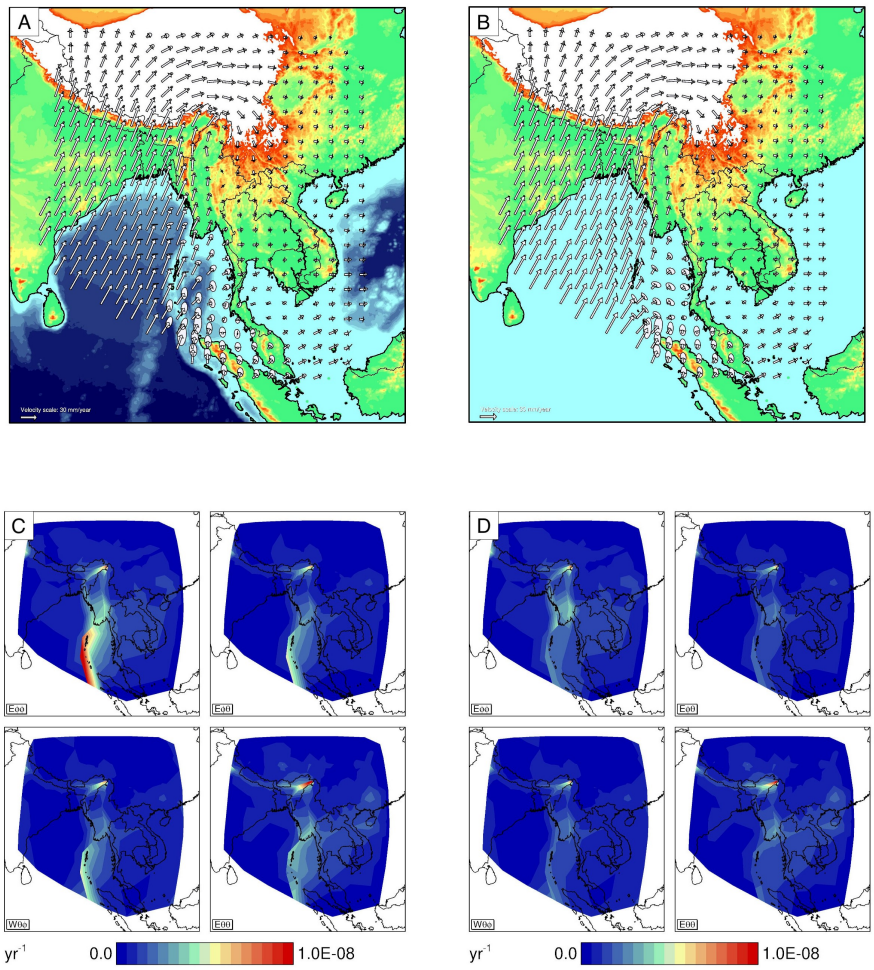

Figure 10: Results of an inversion including both fault slip and continuous deformation (2). A) Velocity prediction before damping. B) Velocity prediction after damping; both A) and B) are a vast improvement over previous models with the only weak part being the southern part of the model (Andaman). C) Model covariance of all four components of the velocity gradient tensor before damping D) Model covariance of all four components after damping; we observe a significant improvement over C) around the Andaman fault system and a small improvement over C) around the Assam block and the EHS.

5.7 The value of using multiple models

Using different models allows us to get a better understanding of the nature behind fault systems. If we take the SF for example; The GPS displacement field suggests a simple shear nature, however, when we look at our results we can observe pure shear in the order of 1.125E-7/y combined with a CW rotation rate of 1.5 to 2.5 °/My for model 3 and pure shear in the order of 0.5E-7/y combined with a near zero rotation rate for model 4b. Furthermore, we can observe a clear trade off of rotation rate and pure strain rate in model 3 against strike slip movement along the SF in model 4b. Combining the aforementioned observations it becomes evident that simple shear can be depicted by a combination of both, pure shear and uniform rotation. Another benefit is the ability to relate strain rates found in model 3 and 4 to fault slip rates found in model 1 and 2 as this gives us a little more insight into the magnitude of convergence/shortening related to the obtained strain rates. Furthermore, going from a continuous deformation model (model 3) to a model where faults are no longer locked (model 4) shows how the inversion partitions between fault motion and continuous deformation. It is also possible that this partitioning results from a subtle technical trade-off between strain rate and fault slip, suggesting a resolution problem. Since this is not easily interpreted from the resolution matrix because of the different physical units of the parameters it may need further investigation in the future.

6 Model interpretation

Model interpretation will be based on the results of an inversion for model 4 after damping. The focus of this interpretation will be with three key regions;the Himalayas, the Tibetan Plateau and Burma.

6.1 Himalayas: uplift and crustal shortening due to active convergence

NE-SW to N-S contraction in the order of 1.5-2.0 E-7 combined with a small normal component of fault slip of 0-4 mm/yr along the Himalayas suggest uplift and crustal shortening due to active convergence between India and Eurasia.

6.2 Tibetan plateau: crustal thinning and uplift due to continental collision

Across the Tibetan Plateau, North of the Himalayas we find mainly E-W extension which gradually transfers into N-S to NE-SW extension in southeastern Tibetan Plateau This is in accordance with the E-W strike of most sinistral strike slip faults and the XXF in both regions respectively. We find a moderate CW rotation rate of up to 2.35°/my which we believe to be mainly accommodated by the XXF seeing how it has a sinistral motion and is located between

the clockwise and anti-clockwise rotating parts of the Eurasian plate. In the east we find E-W orientated contractional strain rate of up to 0.7E-7/y accordant with the strike and location of the LMT. This suggests uplift along the LMT due to collision of the Eurasian plate crust with the rigid Yangtze crust. The type of extension we find in the Tibetan Plateau can be related to crustal thinning which has the underthrusting of the Indian crust in the south and the Yangtze crust in the east as important drivers. The CW rotation rate can also be explained by the NNE orientation of the converging rigid Indian plate and the presence (collision) of a rigid Yangtze plate in the east forcing the weaker Eurasian plate to form faults like the XXF to accommodate all the build up strain.

6.3 Burma: Oblique collision, slab dragging, uplift and crustal shortening due to active convergence

We observe a SW-NE oriented contractional strain rate in the south of Myanmar(Burma) to a more SWW-NEE oriented contractional strain rate of up to 0.8 E-7/y in the center. While the dominance of contractional strain rate in the center suggests uplift of the IBR the significant extensional strain rate components in the South/southeast suggest this region is subjected to less uplift and more lateral displacement (strike slip motion). However, the dominance of SW-NE oriented contractional strain rate and a fault slip normal component of up to 11 mm/yr suggest the RBMT is still accommodating the ongoing convergence between India and Burma. In the North of Burma we can observe an extensional dominant strain rate with a N-S orientation, we can also observe a significant CW rotation rate in the northern part of the Burma plate in the order of 5.7°/my we propose the dragging of the Burma plate by the obliquely colliding Indian plate could be the main driver behind these results. The SF is also likely to play a major role in accommodating this rotation.

7 Discussion & Conclusion

Our strain rate findings in the Himalayas generally agree with the results found by numerous others inluding Pan (2018), Zheng (2017) and Ponraj (2019). Moreover, if we look at model 1 or 2 where we do not measure strain rate but instead focus on fault slip and rotation rate, we can get a sense of the magnitude of convergence related to the build up of strain found in models 3 and 4. Here we find comparable (although slightly lower) values, especially for the West and the East, in the order of 13-17 mm/yr. Our results in the Tibetan plateau add to the case of Liang (2013) who suggested a continuous uplifting of the entire plateau relative to a stable neighboring region in the north. Since the geodynamic setting of the Tibetan plateau was not our main objective we did not include any active faults in this region, therefore our models might be lacking in precision. Nonetheless, our strain rates do seem to agree with those found in Pan (2018) and we can clearly recognize the locations of larger struc-

tures like the XXF system and the LMT in our strain rate and rotation rate fields. For the Burma Terrane the main discrepancies between our results and others are found along the RBMT. We find that the remaining budget (besides SF) is mainly expressed through the RBMT, much like Steckler. However, we do observe a significant strain rate (pure shear) located near the CMF and KBF in model 3, although in model 4b most of this strain rate likely gets translated to fault slip on either the RBMT, the NH or the SF. Nevertheless, since we did not model the CMF or the KBF in detail so our results do not give any conclusive evidence disproving others like Gahalout or Panda & Kundu (2013). Finally we would like to compare our rotation rate field to rotation rates obtained through paleomagnetic data. The CW rotation rate about the EHS is clearly indicated by GPS data, however, how does it compare to paleomagnetic data? Otofuji (2010) shows paleomagnetic data (Figure 11 in appendix A) that indicates one clear area with a CCW rotation and two area's with a CW rotation. CCW rotation of up to 60°is found across the Tibetan plateau while a CW rotation of $<40°$ is found in the Sibumasu block (East adjacent to the SF) and Indochina (denoted "S" in Otofuji) and also in the eastern part of the Quaidam Block ($<20°$, denoted "N" in Otofuji). Li, van Hinsbergen, Deng, Advokaat, and Zhu (2018) also find paleomagnetic evidence confirming a CW rotation of up to 40°in the three rivers region (just East of the EHS) and up to 60°to 80°further south on the Sibumasu block. Westerweel (2009) found a significant CW rotation for the Northern Burma Terrane of $60° \pm 8.7°$. We found a $1.5 - 3.5°$/my CW rotation rate around the EHS while the Burma Terrane shows up to 2.5 °/my in general but has a strong peak near the EHS of 7.6°/my, which translates to rotations of over 150°and 456°respectively if the present rotation is extrapolated to estimate an amount of rotation for the past 60 Myr. This is a lot larger than paleomagnetic data from Otofuji implies. Although still too large, our rotation rate does somewhat agree with the paleomagnetic data found by Li & van Hinsbergen (2018) as their results where based on paleocene data sets, making them significantly younger than the late Cretaceous set used in Otofuji. The largest part of the Tibetan plateau shows a CCW rotation rate in the order of 1.5°/my, although in the north this reaches up to 2.5°/my. This CCW rotation rate is also observed East of the Burma Terrane overlaying a part of the according to paleomagnetic data CW "S" region (Otofuji et al., 2010). Our results translate to 90°and 150°rotations over 60 Myr, which again, but to a lesser extent, is larger than implied by paleomagnetic data and in some cases ("S" region) even opposite from paleogmagnetic data. The present day "N" region seems to be subject to both, a slight CW and a slight CCW rotation although neither seems dominant.

Although multiple discrepancies can be found between paleomagnetic data and ours, the majority of our findings appear to be similar to those of others. Since our extrapolation is based on a fixed tectonic setting These discrepancies could be explained by a change in tectonic setting over time. Therefore, I express confidence in the S-N method as a whole in modelling geodynamical problems based on relative motion data. Even though no major new discoveries where made we did get a slightly better geodynamical view of the Burma

region, albeit how complicated and dependant on smaller scale structures the area likely is to be. The fact that our model without any active faults is nearly as close a fit as our model with active faults adds to the suggestion that the real situation will most likely be an interaction between both,locked and unlocked faults. Unfortunately, we have been unable to find the exact combination as of yet, as we could only afford to look into several large scale faults due to time pressure. Testing the effect of more faults like the CMF and the KBF could expand our views and add to either of the previously mentioned authors cases.

To summarise our findings; we find that a model allowing both fault slip on certain faults (locked NH) and the velocity gradient field describes the data best. We find the following implications:

- Multiple discrepancies between paleomagnetic data and present day rotation rates (e.g. Rotation direction, but not magnitude, of Burma in agreement with paleomagnetic data).
- Active convergence in the Himalayas and the IBR/RBMT with a contractional strain rate of up to 2.0E-7/y and 0.8E-7/y respectively resulting in uplift and crustal shortening in both regions
- Crustal thinning across the central TP with uplift in the East (contractional strain rate of up to 0.7E-7/y) due to collision with a rigid Yangtze plate and a CW rotation rate accommodated by the Xianshuihe-Xiajiang fault system due to NNE movement rigid India and a rigid Yangtze in east
- Oblique active convergence of India-Burma with fault slip of up to 11 mm/y on the western border of Burma indicating at least as much shortening.
- Slab dragging of the Burma plate by the subducting Indian slab as a potential driver for a CW rotation rate

8 Future research

For future research a better representation of important faults like the Xianshuihe-Xiajiang fault system in the Tibetan Plateau, the Churachandpur Mao fault and the Koipoli Fault near the Assam block could help improve our model. Another task that could help improve our model would be to add GPS stations/surveys in NE India (the Shillong-Assam blocks) where we currently have a lack of data. However, due to the deposition of soft sediments by the Brahmaputra river in this region it might pose a challenge to acquire solid locations for these stations/surveys.

9 Acknowledgements

I would like to thank Boris Gesberts for the many many insightful conversations and his guiding role in the early stages of this thesis. I would also like to thank Prof. dr. Spakman for providing lots of input, suggestions and support whenever needed.

10 References

Advokaat, E. and van Hinsbergen, D., 2019, January. Kinematic reconstruction of deformation in SE Asia: unfolding Earth's largest Cenozoic orocline. In Geophysical Research Abstracts (Vol. 21).

Apel, E.V., Burgmann, R. and Banerjee, P., 2008. Indian plate motion, deformation, and plate boundary interactions. AGUFM, 2008, pp.G34A-01.

Argus, D.F., Gordon, R.G. and DeMets, C., 2011. Geologically current motion of 56 plates relative to the no-net-rotation reference frame. Geochemistry, Geophysics, Geosystems, 12(11).

Bos, A.G., Spakman, W. and Nyst, M.C., 2003. Surface deformation and tectonic setting of Taiwan inferred from a GPS velocity field. Journal of Geophysical Research: Solid Earth, 108(B10).

Burg, J.-P., & Bouilhol, P. (2019). Timeline of the South-Tibet–Himalayan belt: The geochronological record of subduction, collision, and underthrusting from zircon and monazite U–Pb ages. Canadian Journal of Earth Sciences, 56(12), 1318–1332 https://doi.org/10.1139/cjes-2018-0174

Collilieux, X., Altamimi, Z., Argus, D.F., Boucher, C., Dermanis, A., Haines, B.J., Herring, T.A., Kreemer, C.W., Lemoine, F.G., Ma, C. and MacMillan, D.S., 2014. External evaluation of the terrestrial reference frame: report of the task force of the IAG sub-commission 1.2. In Earth on the Edge: Science for a Sustainable Planet (pp. 197-202). Springer, Berlin, Heidelberg.

Gahalaut, V.K., Kundu, B., Laishram, S.S., Catherine, J., Kumar, A., Singh, M.D., Tiwari, R.P., Chadha, R.K., Samanta, S.K., Ambikapathy, A. and Mahesh, P., 2013. Aseismic plate boundary in the Indo-Burmese wedge, northwest Sunda Arc. Geology, 41(2), pp.235-238.

Gupta, T.D., Riguzzi, F., Dasgupta, S., Mukhopadhyay, B., Roy, S. and Sharma, S., 2015. Kinematics and strain rates of the Eastern Himalayan Syntaxis from new GPS campaigns in Northeast India. Tectonophysics, 655, pp.15-26.

Henderson, A.L., Najman, Y., Parrish, R., BouDagher-Fadel, M., Barford, D., Garzanti, E. and Andò, S., 2010. Geology of the Cenozoic Indus Basin sedimentary rocks: Paleoenvironmental interpretation of sedimentation from the western Himalaya during the early phases of India-Eurasia collision. Tectonics, 29(6).

Kayal, J.R., Arefiev, S.S., Baruah, S., Hazarika, D., Gogoi, N., Gautam, J.L., Baruah, S., Dorbath, C. and Tatevossian, R., 2012. Large and great earthquakes in the Shillong plateau–Assam valley area of Northeast India Region: Pop-up and transverse tectonics. Tectonophysics, 532, pp.186-192.

Khan, P.K., Shamim, S., Mohanty, M., Kumar, P. and Banerjee, J., 2017. Myanmar-Andaman-Sumatra subduction margin revisited: insights of arc-specific deformations. Journal of Earth Science, 28(4), pp.683-694.

Kreemer, C., Blewitt, G. and Klein, E.C., 2014. A geodetic plate motion and Global Strain Rate Model. Geochemistry, Geophysics, Geosystems, 15(10), pp.3849-3889.

Li, S., van Hinsbergen, D.J., Deng, C., Advokaat, E.L. and Zhu, R., 2018. Paleomagnetic constraints from the Baoshan area on the deformation of the Qiangtang-Sibumasu Terrane around the eastern Himalayan Syntaxis. Journal of Geophysical Research: Solid Earth, 123(2), pp.977-997.

Liang, S., Gan, W., Shen, C., Xiao, G., Liu, J., Chen, W., Ding, X. and Zhou, D., 2013. Three-dimensional velocity field of present-day crustal motion

of the Tibetan Plateau derived from GPS measurements. Journal of Geophysical Research: Solid Earth, 118(10), pp.5722-5732.

Mallick, R., Lindsey, E.O., Feng, L., Hubbard, J., Banerjee, P. and Hill, E.M., 2019. Active convergence of the India-Burma-Sunda plates revealed by a new continuous GPS network. Journal of Geophysical Research: Solid Earth, 124(3), pp.3155-3171.

Mon, C.T., Gong, X., Wen, Y., Jiang, M., Chen, Q.F., Zhang, M., Hou, G., Thant, M., Sein, K. and He, Y., 2020. Insight into major active faults in Central Myanmar and the related geodynamic sources. Geophysical Research Letters, 47(8), p.e2019GL086236.

Mustafar, M.A., Simons, W.J., Tongkul, F., Satirapod, C., Omar, K.M. and Visser, P.N., 2017. Quantifying deformation in North Borneo with GPS. Journal of Geodesy, 91(10), pp.1241-1259.

Nguyen-Van, H., Van Phong, T., Trinh, P.T., Van Liem, N., Thanh, B.N., Pham, B.T., Bui, D.T., Bieu, N., Vinh, H.Q., Xuyen, N.Q. and Tuc, N.D., 2020. Recent tectonics, geodynamics and seismotectonics in the Ninh Thuan Nuclear Power plants and surrounding regions, South Vietnam. Journal of Asian Earth Sciences, 187, p.104080.

Otofuji, Y.I., Yokoyama, M., Kitada, K. and Zaman, H., 2010. Paleomagnetic versus GPS determined tectonic rotation around eastern Himalayan syntaxis in East Asia. Journal of Asian Earth Sciences, 37(5-6), pp.438-451.

Pan, Y., Shen, W.B., Shum, C.K. and Chen, R., 2018. Spatially varying surface seasonal oscillations and 3-D crustal deformation of the Tibetan Plateau derived from GPS and GRACE data. Earth and Planetary Science Letters, 502, pp.12-22.

Panda, D., Kundu, B. and Santosh, M., 2018. Oblique convergence and strain partitioning in the outer deformation front of NE Himalaya. Scientific reports, 8(1), pp.1-9.

Ponraj, M., Amirtharaj, S., Sunil, P.S., Saji, A.P., Kumar, K.V., Arora, S.K., Reddy, C.D. and Begum, S.K., 2019. An assessment of present-day crustal deformation in the Kumaun Himalaya from GPS observations. Journal of Asian Earth Sciences, 176, pp.274-280.

Rao, N.P. and Kumar, M.R., 1999. Evidences for cessation of Indian plate subduction in the Burmese arc region. Geophysical Research Letters, 26(20), pp.3149-3152.

Shewchuk, J.R., 1996, May. Triangle: Engineering a 2D quality mesh generator and Delaunay triangulator. In Workshop on Applied Computational Geometry (pp. 203-222). Springer, Berlin, Heidelberg.

Socquet, A., Vigny, C., Chamot-Rooke, N., Simons, W., Rangin, C. and Ambrosius, B., 2006. India and Sunda plates motion and deformation along their boundary in Myanmar determined by GPS. Journal of Geophysical Research: Solid Earth, 111(B5).

Spakman, W. and Nyst, M.C.J., 2002. Inversion of relative motion data for estimates of the velocity gradient field and fault slip. Earth and Planetary Science Letters, 203(1), pp.577-591.

Spakman, W., van Hinsbergen, D., Fraters, M., Thieulot, C., 2018. Slab dragging, subduction evolution, and slab deformation.

Steckler, M.S., Mondal, D.R., Akhter, S.H., Seeber, L., Feng, L., Gale, J., Hill, E.M. and Howe, M., 2016. Locked and loading megathrust linked to active subduction beneath the Indo-Burman Ranges. Nature Geoscience, 9(8), pp.615-618.

Styron, R., Taylor, M. and Sundell, K., 2015. Accelerated extension of Tibet linked to the northward underthrusting of Indian crust. Nature Geoscience, 8(2), pp.131-134.

Vernant, P., Bilham, R., Szeliga, W., Drupka, D., Kalita, S., Bhattacharyya, A.K., Gaur, V.K., Pelgay, P., Cattin, R. and Berthet, T., 2014. Clockwise rotation of the Brahmaputra Valley relative to India: Tectonic convergence in the eastern Himalaya, Naga Hills, and Shillong Plateau. Journal of Geophysical Research: Solid Earth, 119(8), pp.6558-6571.

Wang, Y., Sieh, K., Tun, S.T., Lai, K.Y. and Myint, T., 2014. Active tectonics and earthquake potential of the Myanmar region. Journal of Geophysical Research: Solid Earth, 119(4), pp.3767-3822.

Westerweel, J., Roperch, P., Licht, A., Dupont-Nivet, G., Win, Z., Poblete, F., Ruffet, G., Swe, H.H., Thi, M.K. and Aung, D.W., 2019. Burma Terrane part of the Trans-Tethyan arc during collision with India according to palaeomagnetic data. Nature geoscience, 12(10), pp.863-868.

Yadav, R.K., Gahalaut, V.K., Bansal, A.K., Sati, S.P., Catherine, J., Gautam, P., Kumar, K. and Rana, N., 2019. Strong seismic coupling underneath Garhwal–Kumaun region, NW Himalaya, India. Earth and Planetary Science Letters, 506, pp.8-14.

Zheng, G., Wang, H., Wright, T.J., Lou, Y., Zhang, R., Zhang, W., Shi, C., Huang, J. and Wei, N., 2017. Crustal deformation in the India-Eurasia collision zone from 25 years of GPS measurements. Journal of Geophysical Research: Solid Earth, 122(11), pp.9290-9312.

11 Appendix A

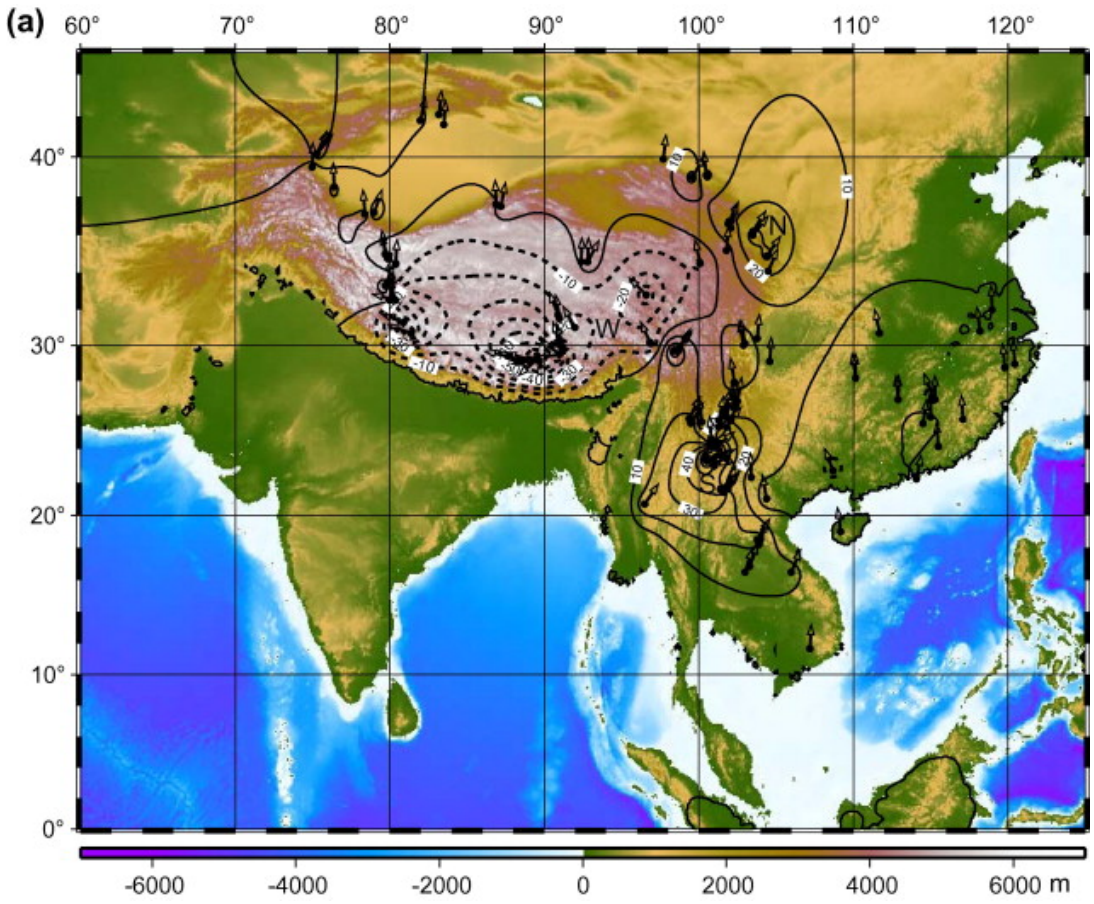

Figure 11: Paleomagnetic data taken from Otofuji (2010): Paleomagnetically determined (long-term) crustal versus present-day tectonic rotation including all data sets. The lines of contours show an amount of rotational motion calculated from reliable paleomagnetic database. An amount of rotation, i.e., a deflection in paleomagnetic declination with respect to north, is shown by arrows. Zones of paleomagnetically determined CW rotation are denoted by "N" and "S", whereas a zone of Paleomagnetically determined CCW rotation is indicated by "W". The bathymetry and land topography are derived from ETOPO2 global dataset (National Geophysical Data Center, 2001).